

# Integration of InSAR Time-Series Analysis and Water-Vapor Correction for Mapping Postseismic Motion After the 2003 Bam (Iran) Earthquake

Zhenhong Li, *Member, IEEE*, Eric J. Fielding, and Paul Cross

**Abstract**—Atmospheric water-vapor effects represent a major limitation of interferometric synthetic aperture radar (InSAR) techniques, including InSAR time-series (TS) approaches (e.g., persistent or permanent scatterers and small-baseline subset). For the first time, this paper demonstrates the use of InSAR TS with precipitable water-vapor (InSAR TS + PWV) correction model for deformation mapping. We use Medium Resolution Imaging Spectrometer (MERIS) near-infrared (NIR) water-vapor data for InSAR atmospheric correction when they are available. For the dates when the NIR data are blocked by clouds, an atmospheric phase screen (APS) model has been developed to estimate atmospheric effects using partially water-vapor-corrected interferograms. Cross validation reveals that the estimated APS agreed with MERIS-derived line-of-sight path delays with a small standard deviation (0.3–0.5 cm) and a high correlation coefficient (0.84–0.98). This paper shows that a better TS of postseismic motion after the 2003 Bam (Iran) earthquake is achievable after reduction of water-vapor effects using the InSAR TS + PWV technique with coincident MERIS NIR water-vapor data.

**Index Terms**—Bam earthquake, interferometry, postseismic motion, synthetic aperture radar (SAR), time series (TS), water-vapor effects.

## I. INTRODUCTION

A MAJOR source of error for repeat-pass interferometric synthetic aperture radar (InSAR) is the phase delay in microwave signal propagation through the atmosphere. The part due to tropospheric precipitable water vapor (PWV) only can cause errors as large as 10–20 cm in deformation retrievals [1]. Reduction of the spatio-temporal variations of InSAR path delays using space-based near-infrared (NIR) water-vapor data [e.g., the NASA Moderate Resolution Imaging Spectroradiometer (MODIS) and the ESA Medium Resolution Imaging Spectrometer (MERIS)] has been successfully demonstrated

[2], [3]: Each model has its natural advantages and inherent limitations, but each is capable of improving the accuracy of InSAR-derived deformation signals from 10 to 5 mm. Although MERIS and MODIS NIR water-vapor products are sensitive to the presence of clouds, they can play an important role in Middle East, North Africa, South Africa, Australia, Chile, Antarctica, Southern California, and North Mexico as these regions show cloud-free frequencies as high as  $\geq 60\%$  [4].

The small-baseline subset algorithm (SBAS) is a robust InSAR time-series (TS) analysis approach, which uses interferograms (Ifms) with small baselines to minimize the effects of baseline decorrelation and inaccuracies in topographic data used [5]–[7]. Unlike persistent scatterer InSAR analysis, phase is unwrapped in 2-D image space first for SBAS rather than in time or in 3-D, making it easy not only to implement in standard interferometric processing but also to integrate with existing water-vapor correction models. The SBAS algorithm is perfect for processing data over arid and urban regions where the coherence is generally high even for long periods with the existing C-band radar archives of ERS, ENVISAT, and RADARSAT-1. Therefore, it appears that the integration of SBAS and MERIS/MODIS water-vapor correction models has the potential for mapping small deformation signals over certain regions (such as the aforementioned desert areas): 1) it has the ability to map surface deformation as it evolves in time, and 2) it is able to better separate transient deformation signals from water-vapor effects. This paper attempts to assess this potential by integrating SBAS with MERIS water-vapor correction model and then applying it to an investigation of the postseismic surface deformation following the 2003  $M_W$  6.6 Bam (Iran) earthquake, using ENVISAT Advanced Synthetic Aperture Radar (ASAR) and MERIS data.

### A. Coseismic and Postseismic Observations for the 2003 Bam (Iran) Earthquake

On December 26, 2003, an  $M_W$  6.6 earthquake devastated the town of Bam, destroying over 50% of its buildings, causing more than 26 000 fatalities, and rendering 100 000 homeless. Previous InSAR studies suggest that the largest magnitude of the fault slip occurred at depth and did not reach the surface. Maximum offsets across the surface ruptures were only 0.25 m, but slip at depth was more than 2 m [8]–[10], which has also been confirmed by other measurements including cross-correlation of optical imagery [11] and leveling data [12]. The stable surface around Bam, combined with low relief and a lack

Manuscript received August 18, 2008; revised February 12, 2009. This work was supported in part by OPA Project 200705003 and NSFC Project 40576044.

This paper has supplementary downloadable material available at <http://ieeexplore.ieee.org>, provided by the authors. This includes a GIF format movie clip, which shows InSAR time-series results for postseismic motions after the 2003  $M_W$  6.6 Bam (Iran) earthquake. This material is 6.4 MB in size.

Z. Li is with the Department of Geographical and Earth Sciences, University of Glasgow, G12 8QQ Glasgow, U.K. (e-mail: zhenhong.li@ges.gla.ac.uk).

E. J. Fielding is with Jet Propulsion Laboratory, California Institute of Technology, Pasadena, CA 91125 USA (e-mail: eric.j.fielding@jpl.nasa.gov).

P. Cross is with the Department of Civil, Environmental and Geomatic Engineering, University College London, WC1E 6BT London, U.K. (e-mail: paul.cross@cege.ucl.ac.uk).

Color versions of one or more of the figures in this paper are available online at <http://ieeexplore.ieee.org>.

Digital Object Identifier 10.1109/TGRS.2009.2019125

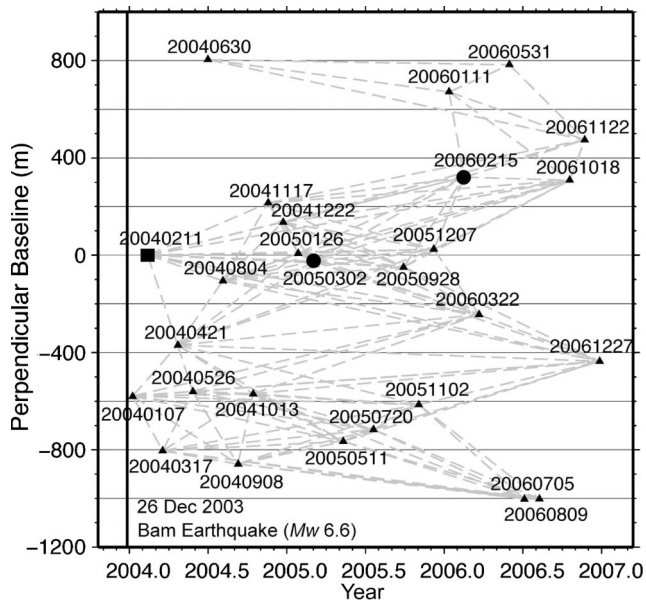


Fig. 1. ENVISAT images from descending track 120: two cloudy dates (denoted by black circles with a label of date in format: YYYYMMDD) and 25 cloud-free dates (denoted by black square and triangles with date labels). The black square marks the reference date for the TS. The reference image was chosen to minimize the atmospheric effects on the TS, because atmospheric delay variations in the reference image will be mapped into all of the other dates. Gray dashed lines, connecting triangles, and dots represent radar Ifms with perpendicular baselines shorter than 400 m. The vertical thick black line indicates the date of the 2003 Bam earthquake.

of vegetation, gives high coherence in the Ifms (even for those with a long temporal baseline of up to three years), which, in turn, provides an outstanding opportunity for InSAR TS analysis.

Standard InSAR TS analysis (without water-vapor correction) showed that the postseismic motion is one order of magnitude smaller than the coseismic deformation and that the signals in individual Ifms were affected strongly by atmospheric variations [13], [14]. These atmospheric effects prevented the measurement of postseismic deformation signals with spatial scales larger than about 10 km where the signal-to-noise ratio was too small.

### B. Data Availability and Interferometric Processing

Fig. 1 and Table I show all 27 ENVISAT ASAR images available in the first three years after the earthquake on descending track 120 (Frame 3015): two were collected under cloudy conditions (indicated by black dots), while 25 were collected under cloud-free conditions (indicated by black square and triangles). Note that descending track ENVISAT data are acquired during the daytime. In this paper, 130 Ifms with a small perpendicular baseline ( $\leq 400$  m) were produced from the 27 ASAR level 0 (raw data) images using the JPL/Caltech ROI\_PAC software (version 2.3) [15], and a subarea around Bam (72 km by 72 km) unwrapped with the SNAPHU program [16].

## II. MERIS INSTRUMENT AND ITS WATER-VAPOR CORRECTION MODEL

MERIS was launched together with the ASAR instrument on the ESA ENVISAT spacecraft on March 1, 2002. MERIS

TABLE I  
ENVISAT IMAGES FROM TRACK 120 (DESCENDING) USED IN THIS PAPER. FOR REFERENCE, DATES ARE GIVEN IN YEAR-MONTH-DAY (YYYYMMDD) FORMAT, AND AS NUMBER OF DAYS SINCE THE EARTHQUAKE. PERPENDICULAR BASELINE IS GIVEN RELATIVE TO THE REFERENCE DATE OF 20040211; THIS REFERENCE DATE WAS CHOSEN BECAUSE OF THE LIMITED ATMOSPHERIC EFFECTS ON THIS CORRESPONDING SAR IMAGE

Image Number	Date (YYYYMMDD)	Number of days	Baseline (m)	Cloud conditions
1	20040107	12	-581	Cloud free
2	20040211	47	0	Cloud free
3	20040317	82	-804	Cloud free
4	20040421	117	-370	Cloud free
5	20040526	152	-561	Cloud free
6	20040630	187	805	Cloud free
7	20040804	222	-106	Cloud free
8	20040908	257	-859	Cloud free
9	20041013	292	-570	Cloud free
10	20041117	327	216	Cloud free
11	20041222	362	136	Cloud free
12	20050126	397	7	Cloud free
13	20050302	432	-26	Cloudy
14	20050511	502	-766	Cloud free
15	20050720	572	-717	Cloud free
16	20050928	642	-49	Cloud free
17	20051102	677	-615	Cloud free
18	20051207	712	25	Cloud free
19	20060111	747	671	Cloud free
20	20060215	782	320	Cloudy
21	20060322	817	-245	Cloud free
22	20060531	887	784	Cloud free
23	20060705	922	-1003	Cloud free
24	20060809	957	-1002	Cloud free
25	20061018	1027	309	Cloud free
26	20061122	1062	474	Cloud free
27	20061227	1097	-436	Cloud free

is a push-broom passive imaging instrument and measures the solar radiation reflected from the Earth's surface and clouds in the visible and NIR spectral range during the daytime with a swath width of 1150 km for the entire 68.5° field of view [17]. MERIS has 15 narrow spectral channels in the near-IR, and the radiance ratio between two of these channels can be used for the remote sensing of water vapor either above land or ocean surfaces under cloud-free conditions [18] or above the highest cloud level under cloudy conditions [19]. The wavelengths of these NIR channels have been chosen by the MERIS science team to minimize the effects of different spectral slopes of the surface. The two channels (i.e., channel 14: 885 nm and channel 15: 900 nm) are only 15 nm apart, and spectral variations of surface reflectance are generally small [18]. In order to further minimize the spectral surface effect, a simple correction algorithm based on the ratio between MERIS channel 10 (753.75 nm) and channel 14 (885 nm) has been implemented in the ESA MERIS water-vapor retrieval algorithm to account for variations in surface albedo spectral slope; a simulation testing indicated a reduction of 25% in the rms error after correction [20]. MERIS NIR water-vapor products are available at two nominal spatial resolutions: 0.3 km for full-resolution (FR) mode and 1.2 km for reduced resolution mode. In [3], MERIS NIR water-vapor products were used to correct water-vapor effects on ENVISAT ASAR Ifms, showing that the order of water-vapor effects on Ifms can be reduced from  $\sim 10$  to  $\sim 5$  mm after correction.

The MERIS NIR water-vapor product has several advantages for correcting ASAR measurements: 1) Because MERIS and ASAR data are acquired simultaneously, there is no difference in timing, and both have a virtually identical propagation path, and 2) MERIS FR mode has a high spatial resolution of up to 300 m.

On the other hand, MERIS NIR water-vapor products are sensitive to the presence of clouds. Because MERIS is limited to wavelengths between 0.4 and 0.9  $\mu\text{m}$  and very valuable thermal measurements with information on liquid and ice water absorption at 1.6 and 3  $\mu\text{m}$  are not available (these bands are used for the NASA MODIS cloud masks), the ESA standard MERIS cloud mask is not “perfect,” particularly when the clouds are thin [3]. A “conservative” cloud mask [3], [21] using the relationship between surface pressure and topography can detect and mask out thin clouds to obtain better water-vapor estimates than those obtained using the ESA official level-2 (L2) cloud-mask product [22].

Over Bam, patches with relatively high water-vapor values were observed in several FR MERIS images, and their spatial patterns were highly correlated from one image to the other. A detailed analysis revealed that their corresponding reflectances (bands 1–7) were negative, implying a bug in the current MERIS NIR water-vapor algorithm, which is being investigated at Free University of Berlin (Rene Preusker, personal communication, 2007). Since the patches always showed consistently larger water-vapor values, a threshold was defined to remove those patches in this paper.

For InSAR atmospheric correction, zenith path delay difference maps (ZPDDMs) have been derived from MERIS data through the following four steps [3].

- 1) MERIS-PWV needs to be converted into zenith wet delay (ZWD) using surface temperature measurements, which were obtained from radiosonde data in this study. Radiosonde data with a temporal sampling of 12 h can be downloaded from the University of Wyoming (<http://weather.uwyo.edu/upperair/sounding.html>).
- 2) A ZPDDM can be calculated by differencing two 2-D ZWD fields (i.e.,  $ZPDDM = ZWD_2 - ZWD_1$ ); note that we are assuming that the zenith dry delay (path delay from the dry part of the atmosphere) has the same spatial distribution and cancels out in the difference map.
- 3) An improved inverse distance weighted interpolation method [23] can be applied to fill in the missing pixels due to the presence of small areas of clouds and/or problematic reflectance values.
- 4) To suppress the inherent noise of MERIS-PWV, a low-pass filter can be applied to the ZPDDM with an average width of 0.6 km for FR MERIS data. Assuming that pixel-to-pixel PWV errors are uncorrelated, the accuracy of the ZPDDM increases by a factor of two at the expense of the spatial resolution.

To reduce water-vapor effects on the Ifms, ZPDDMs are inserted into the interferometric processing sequence after the removal of topographic signals by use of a precise digital elevation model (DEM) such as that produced by the Space Shuttle Radar Topography Mission (SRTM) [24]. The procedure used

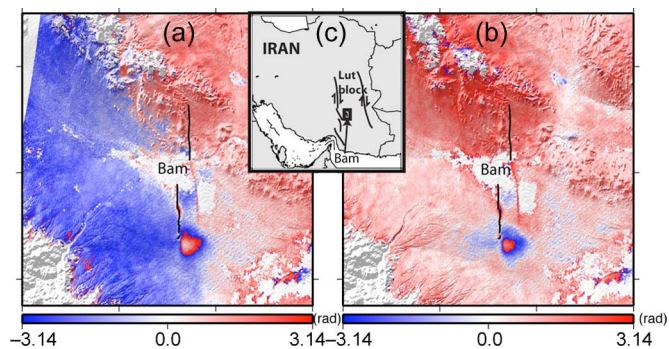


Fig. 2. Rewrapped phases superimposed on an SRTM DEM shown as shaded relief. (a) Original Ifm: 040211–061018. (b) ZPDDM-corrected Ifm using two cloud-free MERIS NIR water-vapor images. The inset shows the location of Bam in southeast Iran. Thick black lines show locations of coseismic fault ruptures mapped from InSAR [9]. The phases are rewrapped so that each  $2\pi$  color cycle from blue to red to blue represents an increase of 2.83 cm in the range from ground to satellite. The width of the area shown is 72 km.

for InSAR water-vapor correction has been successfully incorporated into the JPL/Caltech ROI\_PAC software (readers can refer to [2] and [25] for more details). Fig. 2 shows an example of the MERIS water-vapor correction model. It is clear that the strong gradient from the southwest to the northeast in the original Ifm [Fig. 2(a)] was removed and the real geophysical signals were enhanced after correction [Fig. 2(b)]. In this paper, “ZPDDM-corrected” Ifms refer to those corrected with two cloud-free MERIS NIR water-vapor images.

### III. InSAR TS WITH A WATER-VAPOR CORRECTION MODEL (InSAR TS + PWV)

We have developed a method of inserting water-vapor correction into the SBAS TS analysis method [5]. We start with the standard SBAS formulation [5]. Let  $t$  be a vector of SAR acquisition dates in chronological order. For a data set containing  $N$  Ifms constructed from  $S$  acquisitions on different dates, after removing the flat earth and local topography, the unwrapped differential interferometric phase at pixel  $(x, r)$  computed from the SAR acquisitions at times  $t_M$  (for the master image), the start time, and  $t_S$  (for the slave image), the end time, can be written as follows:

$$\begin{cases} \delta\phi_{t_M t_S}(x, r) = \delta\phi_{t_M t_S}^{\text{topo}}(x, r) + \delta\phi_{t_M t_S}^{\text{disp}}(x, r) \\ \quad + \delta\phi_{t_M t_S}^{\text{atm}}(x, r) + \delta\phi_{t_M t_S}^{\text{noise}}(x, r) \\ \delta\phi_{t_M t_S}^{\text{topo}}(x, r) = \frac{4\pi}{\lambda} \frac{B_{\perp t_M t_S} \Delta Z(x, r)}{r \sin \theta} \\ \delta\phi_{t_M t_S}^{\text{disp}}(x, r) = \frac{4\pi}{\lambda} [d(t_S, x, r) - d(t_M, x, r)] \\ \delta\phi_{t_M t_S}^{\text{atm}}(x, r) = \frac{4\pi}{\lambda} [d_{\text{atm}}(t_S, x, r) - d_{\text{atm}}(t_M, x, r)] \end{cases} \quad (1)$$

where  $\lambda$  is the transmitted signal central wavelength;  $d(t_S, x, r)$  and  $d(t_M, x, r)$  represent the cumulative deformation in the line of sight (LOS) at times  $t_S$  and  $t_M$ , respectively, with respect to the reference instant  $t_0$ , i.e., implying  $d(t_0, x, r) = 0, \forall(x, r)$ ; and  $\Delta Z(x, r)$  is the topographic error present in the DEM used for Ifm generation, and its impact on deformation maps is also a function of the perpendicular baseline component  $B_{\perp t_M t_S}$ , the sensor–target distance  $r$ , and the look angle  $\theta$ . The terms  $d_{\text{atm}}(t_M, x, r)$  and  $d_{\text{atm}}(t_S, x, r)$  account

for temporal atmospheric variations at pixel  $(x, r)$ , and the last term  $\delta\phi_{t_M t_S}^{\text{noise}}(x, r)$  accounts for temporal decorrelation, orbital errors, and thermal noise effects.

In our InSAR TS + PWV analysis, we note that after PWV correction, atmospheric effects on the corrected Ifms are limited, and their residuals can be considered as random noise, so that  $\delta\phi_{t_M t_S}^{\text{atm}}(x, r)$  can be neglected in (1)

$$\begin{cases} \delta\phi_{t_M t_S}^{\text{corr}}(x, r) = \delta\phi_{t_M t_S}^{\text{topo}}(x, r) + \delta\phi_{t_M t_S}^{\text{disp}}(x, r) \\ \quad + \delta\phi_{t_M t_S}^{\text{noise}^2}(x, r) \\ \delta\phi_{t_M t_S}^{\text{corr}}(x, r) = \delta\phi_{t_M t_S}(x, r) - ZPDDM_{t_M t_S} \\ \delta\phi_{t_M t_S}^{\text{noise}^2}(x, r) = \delta\phi_{t_M t_S}^{\text{noise}}(x, r) + \delta\phi_{t_M t_S}^{\text{residual}}(x, r) \end{cases} \quad (2)$$

where  $\delta\phi_{t_M t_S}^{\text{corr}}(x, r)$  represents corrected phase values and  $\delta\phi_{t_M t_S}^{\text{residual}}(x, r)$  represents residual water-vapor effects after correction.

In order to avoid large discontinuities in cumulative deformations and to obtain a physically sound solution, it is usually preferable to use the mean velocities between time-adjacent acquisitions in the network inversion [5]

$$\begin{aligned} \delta\phi_{t_M t_S}^{\text{disp}}(x, r) &= \frac{4\pi}{\lambda} [d(t_S, x, r) - d(t_M, x, r)] \\ &= \frac{4\pi}{\lambda} \sum_{k=M}^{S-1} v_{k,k+1}(t_{k+1} - t_k) \end{aligned} \quad (3)$$

where  $v_{k,k+1}$  is the velocity between the  $k$ th and  $(k+1)$ th time. For a given pixel, let  $V$  be a vector (of size  $(S-1) \times 1$ ) of successive velocities for each interval between dates (i.e.,  $V^T = [v_{0,1} \ v_{1,2} \ \dots \ v_{S-2,S-1}]$ ), let  $Z$  be a parameter of DEM errors, and let  $R$  be a vector of Ifm range changes in the LOS (of size  $N \times 1$ ). Equation (1) can be generalized into a matrix equation for the entire set of Ifms

$$\begin{cases} \begin{bmatrix} T & C \\ N \times (S-1) & N \times 1 \end{bmatrix} \begin{bmatrix} V \\ Z \\ (S-1) \times 1 \end{bmatrix} = \begin{bmatrix} R \\ N \times 1 \end{bmatrix} \\ C^T = \begin{bmatrix} B_{\perp 1} & B_{\perp 2} & \dots & B_{\perp N} \\ r \sin \theta & r \sin \theta & \dots & r \sin \theta \end{bmatrix} \\ R^T = \begin{bmatrix} \frac{\lambda}{4\pi} \delta\phi_1 & \frac{\lambda}{4\pi} \delta\phi_2 & \dots & \frac{\lambda}{4\pi} \delta\phi_N \end{bmatrix} \end{cases} \quad (4)$$

where the  $N \times (S-1)$  matrix  $T$  references time intervals of each Ifm. If all the acquisitions are well connected (i.e., they belong to a single subnetwork), we should have  $N \geq S$ , and  $\begin{bmatrix} T & C \\ N \times (S-1) & N \times 1 \end{bmatrix}$  is an  $S$ -rank matrix. Therefore, (4) is a well-determined ( $N = S$ ) or an overdetermined ( $N > S$ ) system, and its solution can be easily obtained in a least squares sense. Berardino *et al.* [5] also show how solutions can be found for disconnected subnetworks that overlap in time. As shown in Fig. 3, the InSAR TS + PWV technique allows us to map surface deformation as it evolves in time together with a mean velocity field, with a key feature: there is less need for an *a priori* deformation model in InSAR TS analysis with water-vapor correction.

It is clear in Fig. 4 that atmospheric effects can be greatly reduced after using the InSAR TS + PWV technique. However,

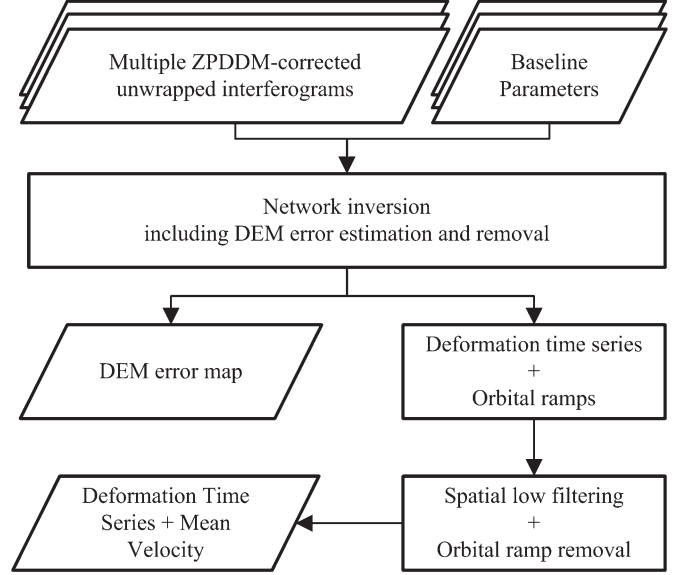


Fig. 3. Flowchart of InSAR TS + PWV without APS.

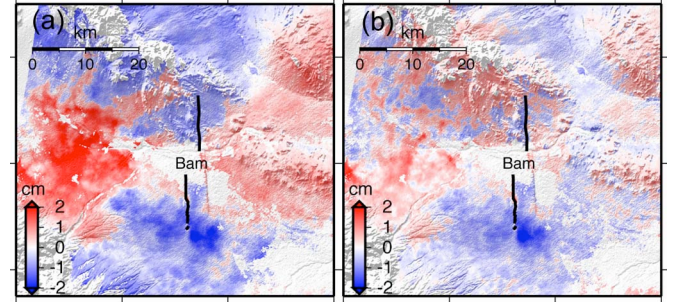


Fig. 4. InSAR TS results. The LOS range changes on date: 20060809 (relative to date: 20040211). (a) Without MERIS water-vapor correction. (b) With MERIS water-vapor correction. Thick black lines show locations of coseismic fault ruptures mapped from InSAR [9].

the temporal resolution (or sampling rate) of the retrieved deformation TS may decrease because the data availability of MERIS NIR water-vapor product is limited due to the presence of clouds. For example, 2 out of 27 MERIS images used in this paper were cloudy ( $\geq 80\%$  cloudy pixels) (Fig. 1). In addition, the January 7, 2004 scene has substantial cloud cover in part of the area of interest. Therefore, we developed an atmospheric phase screen (APS) model to estimate atmospheric effects for a given date using PWV-corrected Ifms.

#### IV. APS MODEL FOR InSAR TS + PWV

##### A. APS Model: Algorithm

In order to make full use of water-vapor data in the APS estimation, a new term, i.e., single-PWV-ZPDDM, is introduced. If water-vapor data are available at time  $t_i$ , but not available at time  $t_j$ , a single-PWV-ZPDDM can be calculated by assuming that ZWD at time  $t_i$  is zero

$$\begin{aligned} \text{Single-PWV-ZPDDM}_{t_i t_j} &= ZWD_{t_j} - ZWD_{t_i} \\ &= ZWD_{t_j} - 0. \end{aligned} \quad (5)$$

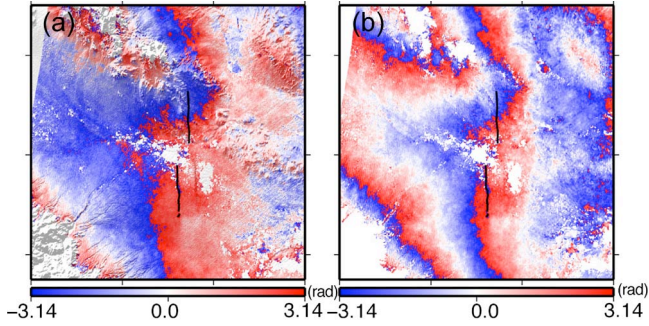


Fig. 5. Rewrapped phases superimposed on shaded-relief SRTM DEM. (a) Original Ifm: 050302–061018. (b) Single-PWV-corrected Ifm using a single cloud-free MERIS NIR water-vapor image collected on 061018. The phases are rewrapped so that each  $2\pi$  color cycle from blue to red to blue represents an increase of 2.83 cm in the range from ground to satellite.

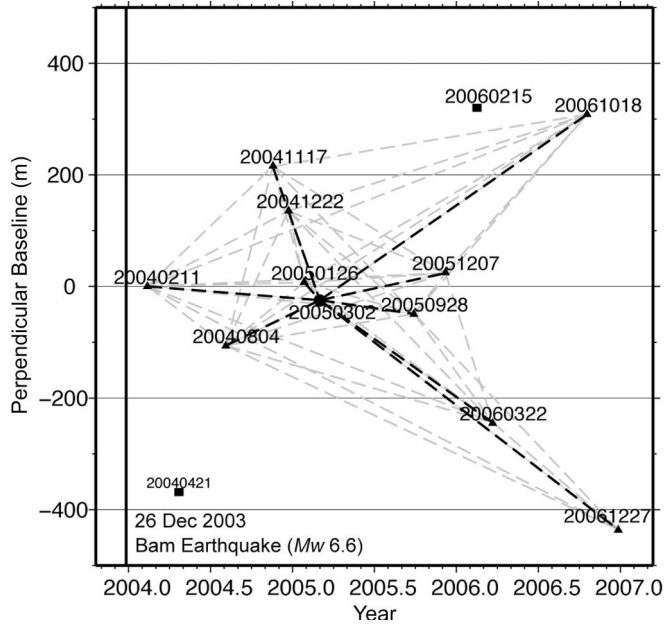


Fig. 6. ENVISAT subnetwork used for estimating the APS on the date of 20050302 (denoted by a black dot). Relative perpendicular baselines are plotted as a function of acquisition dates (format: YYYYMMDD). Black triangles represent the cloud-free dates used in the APS estimation, while black squares indicate the dates not used due to the partial presence of clouds or atmospheric ripples (see text). The 38 dashed gray lines represent ZPDDM-corrected Ifms, while the ten black dashed lines represent single-PWV-corrected Ifms. The solid thick line indicates the date of the Bam earthquake.

As an example, it was cloudy over the Bam region on March 2, 2005, and thus, there was no MERIS NIR water-vapor data on that day. However, a MERIS NIR water-vapor image was available on October 18, 2006. Assuming ZWD on March 2, 2005 to be zero, a single-PWV-corrected Ifm is shown in Fig. 5(b). It is clear that there are about two more fringes in the single-PWV-corrected Ifm [Fig. 5(b)] than the original one [Fig. 5(a)], indicating that, except for deformation signals, topographic artifacts, and orbital errors, the single-PWV-corrected Ifm includes contributions of about two fringes (5.6 cm) from atmospheric effects on March 2, 2005.

In order to estimate atmospheric effects on March 2, 2005, ten single-PWV-corrected Ifms were generated (Fig. 6): 1) the

other date should be cloud free, and 2) the perpendicular baseline should be smaller than 400 m. It should be noted in Fig. 6 that several dates were discarded in the APS estimation due to the partial presence of clouds (e.g., 20060215) or atmospheric ripples (e.g., 20040421). All the cloud-free images in the subnetwork were also combined into 38 ZPDDM-corrected Ifms. By using both types of water-vapor-corrected Ifms, (4) can be expressed as

$$\begin{bmatrix} T & A & C \\ N \times (S-1) & N \times 1 & N \times 1 \end{bmatrix} \begin{bmatrix} V \\ D \\ Z \\ (S-1) \times 1 \\ 1 \times 1 \\ 1 \times 1 \end{bmatrix} = \begin{bmatrix} R \\ N \times 1 \end{bmatrix} \quad (6)$$

where  $D$  is the APS variable for the date of March 2, 2005 and the elements of the  $N \times 1$  vector  $A$  for this specified date  $t_{\text{APS}}$  are given by

$$\begin{cases} A_{t_M t_S} = 0, & (t_M \neq t_{\text{APS}} \text{ and } t_S \neq t_{\text{APS}}) \\ A_{t_M t_S} = -1, & (t_M = t_{\text{APS}} \text{ and } t_S \neq t_{\text{APS}}) \\ A_{t_M t_S} = +1, & (t_M \neq t_{\text{APS}} \text{ and } t_S = t_{\text{APS}}). \end{cases} \quad (7)$$

Based on the fact that the atmospheric signal phase component is highly correlated in space but poorly in time [26], a spatial low-pass filter, together with a temporal high-pass filter, can be used to separate atmospheric effects from deformation signals. This can be easily implemented if a temporal deformation model is known

$$\begin{matrix} V \\ (S-1) \times 1 \end{matrix} = \begin{matrix} M \\ (S-1) \times p \end{matrix} \times \begin{matrix} P \\ p \times 1 \end{matrix} \quad (8)$$

where vector  $P$  contains  $p$  model parameters (typically less than four) and  $M$  is the model matrix describing the velocity vector  $V$ . Hence, (6) can be written as

$$\begin{bmatrix} G & A & C \\ N \times p & N \times 1 & N \times 1 \end{bmatrix} \begin{bmatrix} P \\ D \\ Z \\ p \times 1 \\ 1 \times 1 \\ 1 \times 1 \end{bmatrix} = \begin{bmatrix} R \\ N \times 1 \end{bmatrix} \quad (9)$$

where  $G = \begin{matrix} T \\ N \times p \end{matrix} \times \begin{matrix} M \\ (S-1) \times p \end{matrix}$ . The total number of unknown parameters decreases from  $S + 1$  in (6) to  $p + 2$  in (9) (i.e.,  $p + 2 < S + 1$ , because the number of parameters in the temporal model must be less than the number of dates in the TS for them to be determined by the data) after using the temporal deformation model, and the left-hand matrix in (9) generally turns out to be nonsingular, thus making the equation easy to solve.

It should be noted that characterizing the temporal pattern of deformation is commonly one of the aims of any deformation study, and the assumption of a temporal deformation model will usually have impacts on the separation of deformation signals from atmospheric effects, orbit errors, and other noise (see more discussion in Section IV-B). However, the Bam postseismic motions do appear to be appropriately characterized by a logarithmic function derived from InSAR TS analysis with and

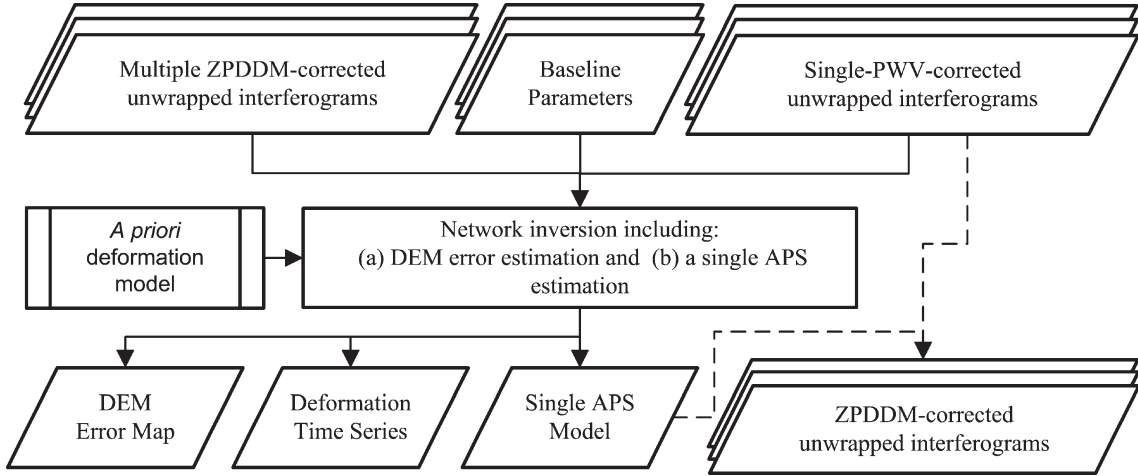


Fig. 7. Flowchart of the APS model for InSAR TS + PWV.

without cloud-free MERIS PWV correction (see Section V and [14] and [27])

$$\begin{aligned} L(\Delta t_i) &= a + b \times \log(t_i - t_{EQ}) \\ &= a + b \times \log(\Delta t_i) \end{aligned} \quad (10)$$

where  $L(\Delta t_i)$  is the range change due to postseismic motions in the LOS at time  $\Delta t_i = t_i - t_{EQ}$  (referenced to the rupture epoch  $t_{EQ}$ ). In this case, the velocity at time  $t_i$  is

$$\begin{aligned} v(t_i) &= \frac{L(\Delta t_{i+1}) - L(\Delta t_i)}{(t_{i+1} - t_i)} \\ &= \frac{\log(\Delta t_{i+1}) - \log(\Delta t_i)}{(t_{i+1} - t_i)} \times b. \end{aligned} \quad (11)$$

Thus, (9) can be expressed as

$$\begin{bmatrix} G \\ N \times 1 \end{bmatrix} \begin{bmatrix} A \\ N \times 1 \end{bmatrix} \begin{bmatrix} C \\ N \times 1 \end{bmatrix} \begin{bmatrix} b \\ 1 \times 1 \\ D \\ 1 \times 1 \\ Z \\ 1 \times 1 \end{bmatrix} = \begin{bmatrix} R \\ N \times 1 \end{bmatrix} \quad (12a)$$

$$\begin{aligned} G_{N \times 1} &= T_{N \times (S-1)} \times M_{(S-1) \times 1} \\ &= T_{N \times (S-1)} \times \left[ \frac{\log(\Delta t_{i+1}) - \log(\Delta t_i)}{(t_{i+1} - t_i)} \right]_{(S-1) \times 1}. \end{aligned} \quad (12b)$$

Note that  $G = T \times M$  is a matrix relating  $N \times 1$  model parameters to observations in (12). Because there is only one model parameter in the logarithmic model [i.e.,  $p = 1$  in (9)], the total number of unknown parameters is three, which can be easily solved in a least squares sense. As shown in Fig. 7, by using the retrieved APS from (12), the single-PWV-corrected Ifms can be further corrected to produce ZPDDM-corrected Ifms that are required in the InSAR TS + PWV analysis.

It should be noted that spatial information has not been taken into account in (9) because it is on a pixel-by-pixel basis.

Assuming that the atmospheric effects on each pixel within a given window ( $K = k \times k$  pixels, where  $k$  is a positive odd and can be determined using pixel sizes and atmospheric correlation distance) are identical, (9) can be expressed as

$$\begin{bmatrix} G_1 & A_1 & C_1 & 0 & \cdots & 0 \\ N \times p & N \times 1 & N \times 1 & N \times 1 & \cdots & N \times 1 \\ G_2 & A_2 & 0 & C_2 & \cdots & 0 \\ N \times p & N \times 1 & N \times 1 & N \times 1 & \cdots & N \times 1 \\ \vdots & \vdots & \vdots & \vdots & \vdots & \vdots \\ G_K & A_K & 0 & 0 & \cdots & C_K \\ N \times p & N \times 1 & N \times 1 & N \times 1 & \cdots & N \times 1 \end{bmatrix} \begin{bmatrix} P \\ p \times 1 \\ D \\ 1 \times 1 \\ Z \\ K \times 1 \end{bmatrix} = \begin{bmatrix} R_1 \\ N \times 1 \\ R_2 \\ N \times 1 \\ \vdots \\ R_K \\ N \times 1 \end{bmatrix}. \quad (13)$$

In (13), the DEM error for each pixel is introduced as an independent unknown parameter. It is clear that when  $K = 1$ , (13) is exactly the same as (9). When  $K > 1$ , the number of unknown parameters slightly increases from  $p + 2$  in (9) to  $p + K + 1$  in (13), while the number of observation equations increases considerably from  $N$  to  $N \times K$ . In this case, (13) is an overdetermined system and can be easily solved in a least squares sense. It is certain that this spatial filter can effectively prevent unphysical oscillatory variations in the APS estimates, but it requires higher computational power and longer computational time.

If no temporal deformation model is known, a temporarily linear velocity (TLV) model can be employed to estimate the APS at time  $t_i$

$$\begin{cases} v_{1,2} = v_{2,3}, & (i = 1) \\ v_{i-1,i} = v_{i,i+1}, & (i \neq 1 \text{ and } i \neq S) \\ v_{S-2,S-1} = v_{S-1,S}, & (i = S). \end{cases} \quad (14)$$

It is clear that the TLV model only makes an assumption on two consecutive intervals and thus has a minimum impact on the whole TS. Following (6), (14) can be rewritten as

$$\begin{bmatrix} F \\ 1 \times (S-1) \end{bmatrix} \begin{bmatrix} 0 \\ 1 \times 1 \end{bmatrix} \begin{bmatrix} 0 \\ 1 \times 1 \end{bmatrix} \begin{bmatrix} V \\ (S-1) \times 1 \\ D \\ 1 \times 1 \\ Z \\ 1 \times 1 \end{bmatrix} = 0. \quad (15)$$

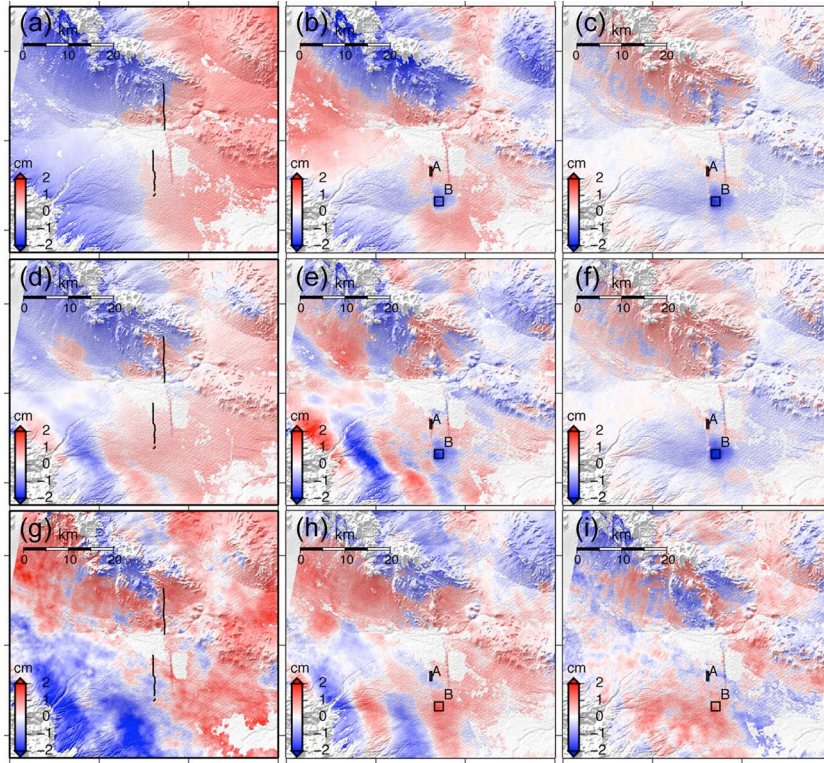


Fig. 8. APS and InSAR TS results (relative to date: 20040211) superimposed on shaded-relief SRTM DEM. (Left column) APS models for dates 20050302, 20060215, and 20040107, respectively. (Middle column) InSAR TS results without APS correction for dates 20050302, 20060215, and 20040107, respectively. (Right column) InSAR TS results with APS correction for dates 20050302, 20060215, and 20040107, respectively. Thick black lines show locations of coseismic fault ruptures mapped from InSAR [9]. The color from blue to white to red implies that the surface moves away from the satellite (except for 20040107 in (h) and (i), i.e., before the reference date, so the sense of time is reversed). Positive values indicate that the pixel exhibits subsidence in the LOS (e.g., the black open rectangle labeled as A). Negative values imply that the pixel exhibits uplift in the LOS (e.g., the black open square labeled as B). Vice versa for (h) and (i).

Combining (6) and (15), we have

$$\begin{bmatrix} T & A & C \\ N \times (S-1) & N \times 1 & N \times 1 \\ F & 0 & 0 \\ 1 \times (S-1) & 1 \times 1 & 1 \times 1 \end{bmatrix} \begin{bmatrix} V \\ D \\ Z \end{bmatrix}_{\begin{matrix} (S-1) \times 1 \\ 1 \times 1 \\ 1 \times 1 \end{matrix}} = \begin{bmatrix} R \\ 0 \\ 1 \end{bmatrix}_{\begin{matrix} N \times 1 \\ 1 \times 1 \\ 1 \times 1 \end{matrix}}. \quad (16)$$

If all the acquisitions are well connected (i.e., they belong to a single subnetwork), we should have  $N \geq S$ , and (16) is a well-determined ( $N + 1 = S + 1$ ) or an overdetermined ( $N + 1 > S + 1$ ) system, and its solution can also be obtained in a least squares sense.

### B. APS Model: Results and Validation

The logarithmic model shown in (10) was employed to estimate APS on a pixel-by-pixel basis in this paper, i.e., no spatial filtering was applied. Fig. 8(a) shows the estimated APS for the date of March 2, 2005 in which an obvious gradient from west to east can be observed. Relative to the InSAR TS result without APS correction [Fig. 8(b)], the one with APS correction [Fig. 8(c)] is much flatter except for the deforming area (indicated by a black open square).

For the dates of February 15, 2006 and January 7, 2004, there are some “ripples” (most likely caused by gravity waves in air flowing over the mountains southwest of Bam) in the estimated APS [Fig. 8(d) and (g)], which are highly correlated with those in the InSAR TS result without correction [Fig. 8(e) and (h)].

It is clear in Fig. 8(f) and (i) that the ripples were completely removed after the APS correction.

To assess the impacts of different deformation models on the APS model, the TLV model was also implemented to estimate the APS for two dates: 20040107 and 20050126. It turned out that the TLV-derived APS estimates agreed to those derived using the logarithmic model with a standard deviation of 0.1 cm for both cases, indicating that the impacts of these two deformation models on the final APS estimates can be neglected. Because the APS model is only applied to a single SAR image without coincident PWV data (or with atmospheric ripple effects) at a time, the impacts of the assumed deformation models are minimized.

In order to validate the APS model, we calculated an APS for cloud-free MERIS scenes and compared it to the slant path delays (SPDs) (i.e., path delays in the satellite LOS) derived from the MERIS NIR water-vapor products. Because the estimated APS includes contributions from orbital errors, it is not appropriate to compare APS with MERIS-derived SPD directly. In this paper, a best fit plane was calculated from the differences between APS and MERIS-derived SPD and then subtracted from the APS. Spatial comparisons were finally performed between the adjusted APS and the MERIS-derived SPD (Fig. 9). High correlation coefficients, 0.84–0.98, were observed with standard deviations of the differences between APS and SPD as small as 0.3–0.5 cm, indicating that the APS model holds promise for estimating water-vapor effects on Ifms.

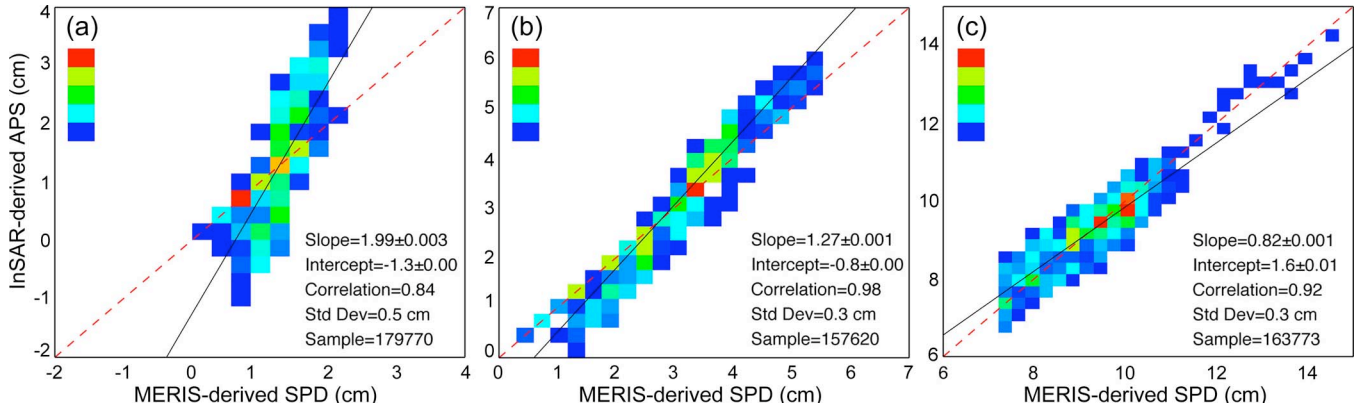


Fig. 9. Comparisons between InSAR-derived APS and MERIS-derived SPD. (a) Date: 20040421 (format: YYYYMMDD). (b) Date: 20050126. (c) Date: 20040107. Note the following: 1) SPD-versus-APS points have been color coded according to density, on a scale ranging from blue, turquoise, green, chartreuse, and red, where red is the maximum; 2) the SPD/APS scale increases for (a)–(c), due to the large temporal water-vapor variations; 3) InSAR-derived APS estimates have been shifted so that they have the same mean value as MERIS-derived SPD; and 4) the dashed red line represents a perfect fit (i.e., unit line), while the solid black line indicates a least squares regression line.

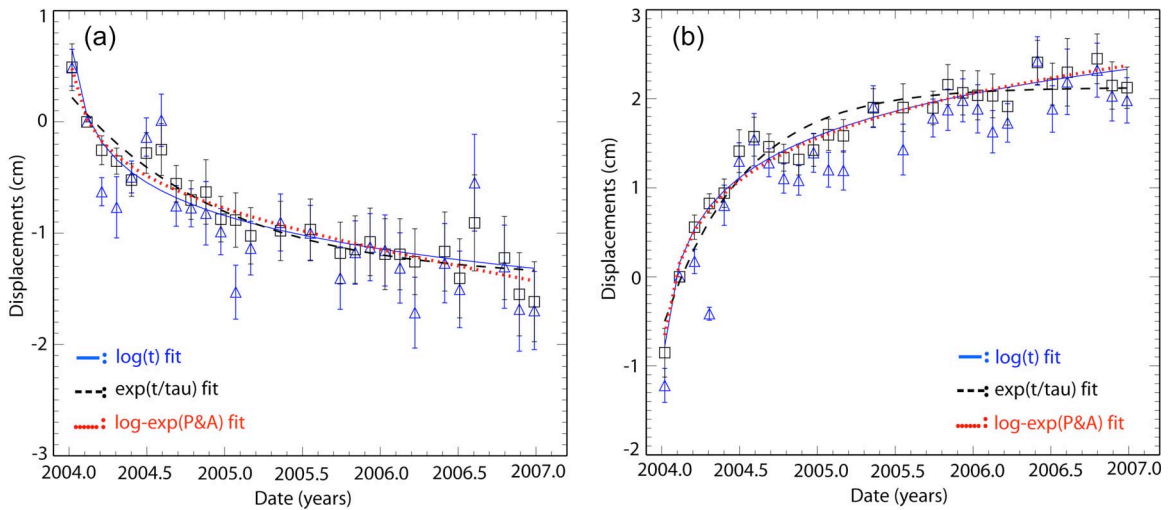


Fig. 10. TS of averages for areas of strong LOS displacements. Blue triangles represent TS without PWV correction, while black squares indicate TS with PWV correction. (a) Area of strong subsidence due to dilatancy recovery [14] ( $0.48 \text{ km} \times 2 \text{ km}$ , black rectangles in Fig. 8). (b) Area of rapid uplift due to afterslip [14] ( $2 \text{ km} \times 2 \text{ km}$ , black squares in Fig. 8). Note the following: 1) formal errors were estimated from rms of the area of interest; 2) fits to points were made with different functions:  $\log(t)$  function (indicated by solid blue lines):  $A + B \times \log(t)$ ;  $\exp(t/\tau)$  function (indicated by dashed black lines):  $A + B \times (1 - e^{-t/\tau})$ ; and  $\log\text{-exp(P\&A)}$  function (indicated by dotted red lines) [29]:  $S + C \times \log(1 + d \times (e^{t/\tau} - 1))$ ; and 3) only the lines fitting the TS with PWV correction are shown.

Assuming the relationship between them to be linear, i.e.,  $APS = a \times SPD + b$ , a least squares fit gives a scale factor and an offset at zero for each case. It is clear in Fig. 9 that the scale factor varied widely from case to case (0.82–1.99) and decreased with an increase in MERIS-derived SPD, i.e., InSAR-derived APS estimates appeared to be greater than MERIS-derived SPD when the amount of atmospheric water vapor was small, while they appeared to be smaller than the latter when the amount of atmospheric water vapor increased. A possible cause of the large variation of the scale factors is orbital errors and hydrostatic (dry air) delays included in the APS estimates.

## V. POSTSEISMIC MOTIONS AFTER THE 2003 $M_W$ 6.6 BAM EARTHQUAKE

The distribution of the postseismic surface deformation indicates that at least two different processes were involved, with

different spatial scales and at different depths in the crust [27]. A narrow zone (roughly 500 m wide) located where the surface ruptures of the 2003 earthquake were observed, south of the city of Bam (black open rectangles in Fig. 8, labeled as A), continued to move away from the descending satellite at least three years after the event [Fig. 10(a)]. Since signals with a similar magnitude can be seen on two ascending tracks (156 and 385, not shown in this paper), the displacement must be vertical [27]. This can be interpreted as localized and shallow compaction of material that dilated during the earthquake [14].

A wider region moving toward the satellite can be observed in the area indicated by black open squares in Fig. 8 (labeled as B), i.e., the southeast end of the main subsurface coseismic rupture inferred from InSAR measurements [28]. Since the ascending tracks (156 and 385) show much smaller signals over a smaller area (not shown in this paper), this displacement must include both uplift and eastward components [27]. Fig. 10 shows that this displacement decays more rapidly with time

TABLE II  
SUMMARY OF FITS TO InSAR TS WITH DIFFERENT FUNCTION FORMS

Region	Function <sup>1</sup>	InSAR TS (no correction)		InSAR TS + PWV	
		Decay time (yr)	RMS (cm)	Decay time (yr)	RMS (cm)
A <sup>2</sup>	log(t)	-	0.29	-	0.14
	exp(t/tau)	0.84	0.29	0.99	0.14
	log-exp(P&A)	2.59	0.28	1.41	0.13
B <sup>3</sup>	log(t)	-	0.27	-	0.14
	exp(t/tau)	0.56	0.29	0.51	0.19
	log-exp(P&A)	9.70	0.27	9.24	0.15

Note: <sup>1</sup>: Function forms: log(t) function:  $A + B \times \log(t)$ ; exp(t/tau) function:  $A + B \times (1 - e^{t/\tau})$ ; and log-exp(P&A) function [29]:  $S + C \times \log(1 + d \times (e^{t/\tau} - 1))$ ;

<sup>2</sup>: Subsidence region indicated by a black open rectangle (with a label of A) in Fig. 8;

<sup>3</sup>: Uplift region indicated by a black open square (with a label of B) in Fig. 8.

than the shallow compaction. The displacement is believed to be due to afterslip above and to the south of the main coseismic slip asperity that ruptured during the 2003 earthquake [14].

It is shown in Fig. 10 that InSAR TS (with and without PWV correction) can be fitted with three different functions that have been used for postseismic processes: 1) log( $t$ ) function:  $A + B \times \log(t)$ ; 2) exp( $t/\tau$ ) function:  $A + B \times (1 - e^{t/\tau})$ ; and 3) log-exp(P&A) “Perfettini & Avouac” function [29]:  $S + C \times \log(1 + d \times (e^{t/\tau} - 1))$ , where  $A$ ,  $B$ ,  $S$ ,  $C$ ,  $d$ , and  $\tau$  are constants and  $t$  is time in years since the earthquake (note that  $\tau$  is different in (2) and (3) functions). Strong variations can be observed in the InSAR TS without PWV correction, with a misfit rms of 0.27–0.29 cm, in both the shallow compaction [Fig. 10(a)] and the afterslip regions [Fig. 10(b)]. In contrast, the InSAR TS + PWV TS appeared to have a smaller misfit rms of 0.13–0.19 cm (i.e., about 50% in reduction) in both deformation regions. In Table II, changes in the estimated decay times can be observed after applying water-vapor correction, particularly for the shallow compaction region (labeled as A), e.g., the decay time for the log-exp(P&A) function is 2.59 years without PWV correction, while it decreases to 1.41 years with PWV correction.

Despite the significant reduction in the atmospheric errors after the PWV corrections, it was still not possible in this case to determine which of the three postseismic time functions fits the data best (see Fig. 10 and Table II), primarily because the first ASAR image was acquired 12 days after the earthquake [14]. An InSAR satellite with a shorter repeat interval would have better resolved the time function.

## VI. DISCUSSION AND CONCLUSION

As shown in Fig. 8(e) and (h), atmospheric ripples with a wavelength of 3–5 km can be observed in four out of the total 27 ASAR images used in this paper, of which three have coincident MERIS data available (e.g., 20040107 and 20050126). Similar short-wavelength signals can be seen in the MERIS water-vapor data for those three days, owing to their high spatial resolution (up to 300 m). This indicates that these signals resulted from

spatial variations of the water vapor. Because atmospheric ripples can be easily identified due to their large amplitudes and short wavelengths, a proper selection of Ifms (e.g., excluding those with obvious atmospheric ripples) makes it possible to reduce the impacts of atmospheric ripples to a minimum at an expense of temporal resolution in InSAR TS analysis. We have shown that residual water-vapor effects are small in the selected ZPDDM-corrected Ifms, and no *a priori* deformation model is required to estimate spatially dense deformation TS as well as a mean deformation map, which is the key advantage of the InSAR TS + PWV approach.

By using the deformation TS from the TS analysis with the properly selected ZPDDM-corrected Ifms, a temporal deformation model can be derived and then used for estimating the APS for a given date. Alternatively, the TLV model can be adopted in the APS estimation. It is evident that the APS model proposed in this paper cannot only reduce long-wavelength but also short-wavelength water-vapor effects on the InSAR TS results (Fig. 8 and supplementary GIF movie).<sup>1</sup> Since the APS model is only applied to a single SAR image without coincident PWV data (or with atmospheric ripple effects) at a time, the impacts of the assumed deformation models (or temporal filter) on the final TS results are minimized (see Section IV-B), which is another key advantage of the InSAR TS + PWV approach over several existing InSAR TS techniques. It should be noted that the extent to which the impacts of the assumed deformation models can

<sup>1</sup>This paper has supplementary downloadable material available at <http://ieeexplore.ieee.org>, provided by the authors. This includes a GIF format movie clip, which shows InSAR time-series results for postseismic motions after the 2003 M<sub>W</sub> 6.6 Bam (Iran) earthquake: (a) without water-vapor correction and (b) with water-vapor correction. Note the following: 1) thick black lines show locations of coseismic fault ruptures mapped from InSAR [9]; 2) the 20040211 image was chosen as the reference for the time-series analysis due to its limited atmospheric effects, so it has zero values by definition; 3) the color from blue to white to red implies that the surface moves away from the satellite except for the date of 20040107 (because it is before the reference date, the sign of its postseismic deformation is opposite to the others); and 4) except for the date of 20040107, positive values indicate that the pixel exhibits subsidence in the LOS, e.g., the area labeled as A; negative values imply that the pixel exhibits uplift in the LOS, e.g., the area indicated by the black open square and labeled as B. This material is 6.4 MB in size.

be depends on two factors: The first factor is the time intervals between the date of interest and its two neighboring dates. The shorter the intervals, the smaller the impacts will be. The second factor is the actual deformation pattern during the period spanned by the date of interest and its two neighboring dates. When the change in the temporal deformation pattern is small, the impacts of the assumed deformation models (e.g., the TLV model) can be trivial.

The performance of the APS model also depends on the structure of the SAR subnetwork (Fig. 7): 1) The black dot (i.e., the APS date) is preferably located in the center of the subnetwork in order to optimize the estimation of the deformation model parameters; in other words, the greatest impacts of uncertainties in the deformation model on the APS estimates occur if the black dot is located at either end of the subnetwork (i.e., either the first or the last date—this is especially true for the first date with the  $\log(t)$  time function because of its inherent feature; its displacement velocity sharply decreases with time, and there is a large uncertainty in the exact amount of curvature in the time function, so extrapolation to the first date has larger errors), and 2) the more baselines (i.e., ZPPDM-corrected and single-PWV-corrected Ifms), the more robust the subnetwork, and the better the APS solution is expected to be. This indicates that water-vapor data availability is an issue that should be considered. MERIS and MODIS near-infrared water-vapor data sets are usable only under cloud-free conditions and during the day, while dense continuous GPS networks are currently only available in certain regions (e.g., Southern California and Japan). Since numerical weather models (NWMs) can provide estimates of tropospheric path delays with a global coverage, 24 h a day in all weather, it is likely that the use of NWM will expand the application of the InSAR TS + PWV approach for deformation mapping, which will be an important issue in future work.

#### ACKNOWLEDGMENT

The authors would like to thank J. Biggs, T. Wright, A. Sibthorpe, and P. Lundgren for the useful discussions and also P. Lundgren for sharing his SBAS codes (in Matlab) that inspired this study. The GMT mapping software [30] was used to prepare some figures. This work was carried out within the NERC Earth Observation Centre of Excellence: Centre for the Observation and Modelling of Earthquakes and Tectonics. Part of this work was carried out at Jet Propulsion Laboratory, California Institute of Technology, under contract with the National Aeronautics and Space Administration. The ENVISAT ASAR and MERIS data are copyright 2004–2006 by the European Space Agency and were provided under projects AOE.668 and C1P.3336.

#### REFERENCES

- [1] H. A. Zebker, P. A. Rosen, and S. Hensley, "Atmospheric effects in interferometric synthetic aperture radar surface deformation and topographic maps," *J. Geophys. Res.*, vol. 102, no. B4, pp. 7547–7563, 1997.
- [2] Z. Li, J.-P. Muller, P. Cross, and E. J. Fielding, "Interferometric synthetic aperture radar (InSAR) atmospheric correction: GPS, Moderate Resolution Imaging Spectroradiometer (MODIS), and InSAR integration," *J. Geophys. Res.*, vol. 110, no. B3, p. B03410, 2005. DOI:10.1029/2004JB003446.
- [3] Z. Li, E. J. Fielding, P. Cross, and J.-P. Muller, "Interferometric synthetic aperture radar atmospheric correction: Medium Resolution Imaging Spectrometer and Advanced Synthetic Aperture Radar integration," *Geophys. Res. Lett.*, vol. 33, no. 6, p. L06816, Mar. 2006. DOI:10.1029/2005GL025299.
- [4] Z. Li, E. J. Fielding, P. Cross, and R. Preusker, "Advanced InSAR atmospheric correction: MERIS/MODIS combination and stacked water vapour models," *Int. J. Remote Sens.*, 2009, to be published.
- [5] P. Berardino, G. Fornaro, R. Lanari, and E. Sansosti, "A new algorithm for surface deformation monitoring based on small baseline differential SAR interferograms," *IEEE Trans. Geosci. Remote Sens.*, vol. 40, no. 11, pp. 2375–2383, Nov. 2002.
- [6] R. Lanari, F. Casu, M. Manzo, G. Zeni, P. Berardino, M. Manunta, and A. Pepe, "An overview of the small baseline subset algorithm: A DInSAR technique for surface deformation analysis," *Pure Appl. Geophys.*, vol. 164, no. 4, pp. 637–661, Apr. 2007.
- [7] O. Mora, J. J. Mallorqui, and A. Broquetas, "Linear and nonlinear terrain deformation maps from a reduced set of interferometric SAR images," *IEEE Trans. Geosci. Remote Sens.*, vol. 41, no. 10, pp. 2243–2253, Oct. 2003.
- [8] J. Jackson, M. Bouchon, E. Fielding, G. J. Funning, M. Ghorashi, D. Hatzfeld, H. Nazari, B. Parsons, K. Priestley, M. Talebian, M. Tatar, R. Walker, and T. J. Wright, "Seismotectonic, rupture process, and earthquake-hazard aspects of the 2003 December 26 Bam, Iran, earthquake," *Geophys. J. Int.*, vol. 166, no. 3, pp. 1270–1292, Sep. 2006.
- [9] E. J. Fielding, M. Talebian, P. A. Rosen, H. Nazari, J. A. Jackson, M. Ghorashi, and M. Berberian, "Surface ruptures and building damage of the 2003 Bam, Iran, earthquake mapped by satellite synthetic aperture radar interferometric correlation," *J. Geophys. Res.*, vol. 110, no. B3, p. B03302, Mar. 2005. DOI: 10.1029/2004JB003299.
- [10] M. Talebian, E. J. Fielding, G. Funning, M. Ghorashi, J. A. Jackson, H. Nazari, B. E. Parsons, K. Priestley, P. A. Rosen, and R. Walker, "The 2003 Bam (Iran) earthquake: Rupture of a blind strike-slip fault," *Geophys. Res. Lett.*, vol. 31, no. 11, p. L11611, 2004. DOI: 10.1029/2004GL020058.
- [11] M. Peyret, J. Chéry, Y. Djamour, A. Avallone, F. Sarti, P. Briole, and M. Sarpoulaki, "The source motion of 2003 Bam (Iran) earthquake constrained by satellite and ground-based geodetic data," *Geophys. J. Int.*, vol. 169, no. 3, pp. 849–865, Jun. 2007.
- [12] M. Motagh, J. Klotz, F. Tavakoli, Y. Djamour, S. Arabi, H.-U. Wetzel, and J. Zschau, "Combination of precise leveling and InSAR data to constrain source parameters of the Mw = 6.5, 26 December 2003 Bam earthquake," *Pure Appl. Geophys.*, vol. 163, no. 1, pp. 1–18, Jan. 2006.
- [13] E. Fielding, P. Lundgren, G. Funning, R. Burgmann, Z. Li, and E. Pathier, "Earthquake and fault interactions in Southwest Asia, from SAR interferometry and image offsets," in *ESA ENVISAT Symp.*, Montreux, Switzerland, Apr. 23–27, 2007.
- [14] E. J. Fielding, P. R. Lundgren, R. Bürgmann, and G. J. Funning, "Shallow fault-zone dilatancy recovery after the 2003 Bam, Iran earthquake," *Nature*, vol. 458, no. 7234, pp. 64–68, Mar. 2009.
- [15] P. A. Rosen, S. Hensley, G. Peltzer, and M. Simons, "Updated repeat orbit interferometry package released," *EOS Trans. AGU*, vol. 85, no. 5, p. 47, 2004.
- [16] C. W. Chen and H. A. Zebker, "Network approaches to two-dimensional phase unwrapping: Intractability and two new algorithms," *J. Opt. Soc. Amer. A, Opt. Image Sci. Vis.*, vol. 17, no. 3, pp. 401–414, Mar. 2000.
- [17] ESA-MERIS, *MERIS Product Handbook*, 2004. Issue 1.3.
- [18] R. Bennartz and J. Fischer, "Retrieval of columnar water vapour over land from back-scattered solar radiation using the Medium Resolution Imaging Spectrometer (MERIS)," *Remote Sens. Environ.*, vol. 78, pp. 271–280, 2001.
- [19] P. Albert, R. Bennartz, and J. Fischer, "Remote sensing of atmospheric water vapor from backscattered sunlight in cloudy atmospheres," *J. Atmos. Ocean. Technol.*, vol. 18, no. 6, pp. 865–874, Jun. 2001.
- [20] J. Fischer and R. Bennartz, "Retrieval of total water vapour content from MERIS measurements," ESA-ESTEC, Noordwijk, The Netherlands, 1997. ESA reference number PO-TN-MEL-GS-005, Algorithm Theoretical Basis Document (ATBD).
- [21] D. Ramon, L. Cazier, and R. Santer, "Surface pressure product accuracy with respect to cloud flagging," in *Working Meeting MERIS AATSR Calibration Geophys. Validation (MAVT)*, Oct. 20–24, 2003. [Online]. Available: [http://envisat.esa.int/workshops/mavt\\_2003/MAVT-2003\\_503-paper\\_DRamon.pdf](http://envisat.esa.int/workshops/mavt_2003/MAVT-2003_503-paper_DRamon.pdf)

- [22] R. Santer, V. Carrère, D. Dessailly, P. Dubuisson, and J. Rogerin, "MERIS algorithm theoretical basis document (ATBD 2.17). Pixel identification," ESA, Paris, France, 1997.
- [23] Z. Li, "Production of regional 1 km  $\times$  1 km water vapor fields through the integration of GPS and MODIS data (Winner of Student Paper Prize & Best Paper Presentation)," in *ION GNSS*, Long Beach, CA, Sep. 21–24, 2004, pp. 2396–2403.
- [24] T. G. Farr, P. A. Rosen, E. Caro, R. Crippen, R. Duren, S. Hensley, M. Kobrick, M. Paller, E. Rodriguez, L. Roth, D. Seal, S. Shaffer, J. Shimada, J. Umland, M. Werner, M. Oskin, D. Burbank, and D. Alsdorf, "The Shuttle Radar Topography Mission," *Rev. Geophys.*, vol. 45, no. 2, p. RG2004, 2007. DOI: 10.1029/2005RG000183.
- [25] Z. Li, E. J. Fielding, P. Cross, and J.-P. Muller, "Interferometric synthetic aperture radar atmospheric correction: GPS topography-dependent turbulence model," *J. Geophys. Res.*, vol. 111, no. B2, p. B02404, 2006. DOI: 10.1029/2005JB003711.
- [26] A. Ferretti, C. Prati, and F. Rocca, "Nonlinear subsidence rate estimation using permanent scatterers in differential SAR interferometry," *IEEE Trans. Geosci. Remote Sens.*, vol. 38, no. 5, pp. 2202–2212, Sep. 2000.
- [27] E. J. Fielding, P. Lundgren, Z. Li, G. Funning, and R. Bürgmann, "Post-seismic deformation after the 2003 Bam, Iran earthquake from time series analysis of Envisat InSAR," in *SSA Annu. Meeting*, San Francisco, CA, Apr. 18–22, 2006.
- [28] G. J. Funning, B. Parsons, T. J. Wright, J. A. Jackson, and E. J. Fielding, "Surface displacements and source parameters of the 2003 Bam (Iran) earthquake from Envisat Advanced Synthetic Aperture Radar imagery," *J. Geophys. Res.*, vol. 110, no. B9, p. B09406, Sep. 2005. DOI:10.1029/2004JB003338.
- [29] H. Perfettini and J.-P. Avouac, "Postseismic relaxation driven by brittle creep: A possible mechanism to reconcile geodetic measurements and the decay rate of aftershocks, application to the Chi-Chi earthquake, Taiwan," *J. Geophys. Res.*, vol. 109, no. B2, p. B02304, Feb. 2004. DOI: 10.1029/2003JB002488.
- [30] P. Wessel and W. H. F. Smith, "New, improved version of the Generic Mapping Tools released," *EOS Trans. AGU*, vol. 79, no. 47, p. 579, 1998.



**Eric J. Fielding** received the A.B. degree in earth sciences from Dartmouth College, Hanover, NH, and the Ph.D. degree in geological sciences from Cornell University, Ithaca, NY.

Since 1994, he has been a Research Scientist with the Jet Propulsion Laboratory, California Institute of Technology, Pasadena. He was also a Research Scientist with the University of Oxford, Oxford, U.K., and a Visiting Research Scientist with the University of Cambridge, Cambridge, U.K. His current research interests include the application of synthetic aperture radar interferometry to measuring deformation on and around faults before, during, and after earthquakes.

Dr. Fielding is a member of the American Geophysical Union and Geological Society of America.



**Paul Cross** received the B.Sc. degree in civil engineering and the Ph.D. degree in geodesy from the University of Nottingham, Nottingham, U.K., in 1967 and 1970, respectively.

He is currently a Professor of space geodesy with the Department of Civil, Environmental and Geomatic Engineering, University College London (UCL), London, U.K. Before joining UCL in 1997, he held teaching and research positions with the Universities of Nairobi, East London, Stuttgart, and Newcastle. His main research interests include precise GPS positioning and InSAR deformation measurement, and he currently concentrates on engineering and geophysical applications.

Prof. Cross is a member of the American Geophysical Union and the U.K. Remote Sensing and Photogrammetry Society.



**Zhenhong Li (M'07)** received the B.Sc. degree (with distinction) in geodesy from the Wuhan Technical University of Surveying and Mapping (now Wuhan University), Wuhan, China, in 1997, and the Ph.D. degree in GPS, geodesy, and navigation from University College London, London, U.K., in 2005.

Since 2008, he has been a Lecturer in surveying and geodesy with the Department of Geographical and Earth Sciences, University of Glasgow, Glasgow, U.K. His main research interest is the use of space geodesy (including InSAR and GPS) for monitoring

the Earth's surface deformation, and he specializes in InSAR atmospheric correction models. He is currently working on the detection of small-surface movements using InSAR time-series techniques.

Dr. Li is a member of the American Geophysical Union and the U.K. Remote Sensing and Photogrammetry Society.